ACTUATORS

A ferrobotic system for automated microfluidic logistics

Wenzhuo Yu[1]*, Haisong Lin[1]*, Yilian Wang[2]*, Xu He[1], Nathan Chen[1], Kevin Sun[1], Darren Lo[2], Brian Cheng[2], Christopher Yeung[1], Jiawei Tan[1], Dino Di Carlo[2†], Sam Emaminejad[1,2†]

Automated technologies that can perform massively parallelized and sequential fluidic operations at small length scales can resolve major bottlenecks encountered in various fields, including medical diagnostics, -omics, drug development, and chemical/material synthesis. Inspired by the transformational impact of automated guided vehicle systems on manufacturing, warehousing, and distribution industries, we devised a ferrobotic system that uses a network of individually addressable robots, each performing designated micro-/nanofluid manipulation-based tasks in cooperation with other robots toward a shared objective. The underlying robotic mechanism facilitating fluidic operations was realized by addressable electromagnetic actuation of miniature mobile magnets that exert localized magnetic body forces on aqueous droplets filled with biocompatible magnetic nanoparticles. The contactless and high-strength nature of the actuation mechanism inherently renders it rapid (~10 centimeters/second), repeatable (>10,000 cycles), and robust (>24 hours). The robustness and individual addressability of ferrobots provide a foundation for the deployment of a network of ferrobots to carry out cross-collaborative logistics efficiently. These traits, together with the reconfigurability of the system, were exploited to devise and integrate passive/active advanced functional components (e.g., droplet dispensing, generation, filtering, and merging), enabling versatile system-level functionalities. By applying this ferrobotic system within the framework of a microfluidic architecture, the ferrobots were tasked to work cross-collaboratively toward the quantification of active matrix metallopeptidases (a biomarker for cancer malignancy and inflammation) in human plasma, where various functionalities converged to achieve a fully automated assay.

INTRODUCTION

The advent of Industry 4.0 is pioneered by automated guided vehicles (AGVs) that are widely used in distribution and supply chain logistics to perform autonomous, accurate, and consistent cargo transportation while reducing transit times and labor costs (*1*). The flexibility and scalability of such mobile automated systems, in conjunction with their ability to assign specific tasks to individual vehicles cooperating in a large network, provide new degrees of automation in comparison with physically constrained conveyor belt or forklift-operated systems (*2*). The same degrees of automation are poised to revolutionize applications such as medical diagnostics (*3*, *4*), -omics (*5*–*7*), drug development (*8*), and chemical/material synthesis (*9*). In that regard, the full potential of these applications can be unlocked by adopting solutions centering on microfluidic logistics, herein defined as the detailed coordination of diverse, large-scale, and small-volume fluid handling operations to perform a plethora of sample processing and analysis tasks.

To this end, conventional continuous-flow microfluidic systems have shown high throughput and robust fluid handling capabilities (*10*–*12*). However, their predefined fluid pathways and geometrically constrained operations severely limit their adaptability and automation, imposing the same limitations as conveyor belt systems within larger-scale settings. Aiming to resolve such constraints, digital microfluidic actuation techniques such as electrowetting-on-dielectric (EWOD) have emerged, capable of transporting discrete droplets on an open surface in a programmable fashion (*13*–*15*). However, inherent limitations of EWOD devices, stemming from the reliance on direct interactions between the solution and the electrified surfaces, can restrict their service life and compatibility with other peripheral components, thus narrowing their application diversity (*16*, *17*).

Here, inspired by the transformational impact of automated guided robotic systems on the manufacturing and distribution industries, we devised a robotic system that uses a network of individually addressable robots, each performing designated micro-/nanofluid manipulation-based tasks in cooperation with other robots. As illustrated in Fig. 1A, analogous to a standard AGV system—which consists of three primary entities, including a navigation floor, an electric motor, and a cargo carrier for package delivery—our robotic system can be described as: (i) an electromagnetic (EM) navigation floor, which can be programmed to establish localized EM fields in an addressable matrix of coils; (ii) a millimeter-scale permanent magnet as a motor, the movement of which is controlled by the activated EM field(s); and (iii) a ferrofluid droplet carrier, encapsulating the bio/chemical sample of interest (i.e., the "package") that is set in motion upon experiencing strong body forces originating from the interaction of the ferrofluid's magnetic nanoparticle constituents with the motor's magnetic actuation field.

Effectively, the devised design leverages EM induction to achieve scalable control, and an intermediary EM-controlled permanent magnet to amplify the actuation field exerted on the ferrofluid (Fig. 1B). In this way, we overcame the fundamental limitations of previously reported magnetic digital microfluidics, which used complex translational stages and bulky magnets that were not portable (*18*, *19*) or EM coils (*20*, *21*) that lacked the ample driving forces to execute efficient fluid operations. The addressability and strength of the ferrofluid actuation enable new degrees of mobility and automation central to the devised robotic system, hereafter referred to as "ferrobotic system."

The contactless and high-strength nature of the ferrobotic actuation mechanism inherently renders it rapid, repeatable, and robust.

[1]Interconnected & Integrated Bioelectronics Lab (I²BL), Department of Electrical and Computer Engineering, University of California, Los Angeles, CA, USA. [2]Department of Bioengineering, University of California, Los Angeles, CA, USA.
*These authors contributed equally to this work.
†Corresponding author. Email: emaminejad@ucla.edu (S.E.); dicarlo@ucla.edu (D.D.)

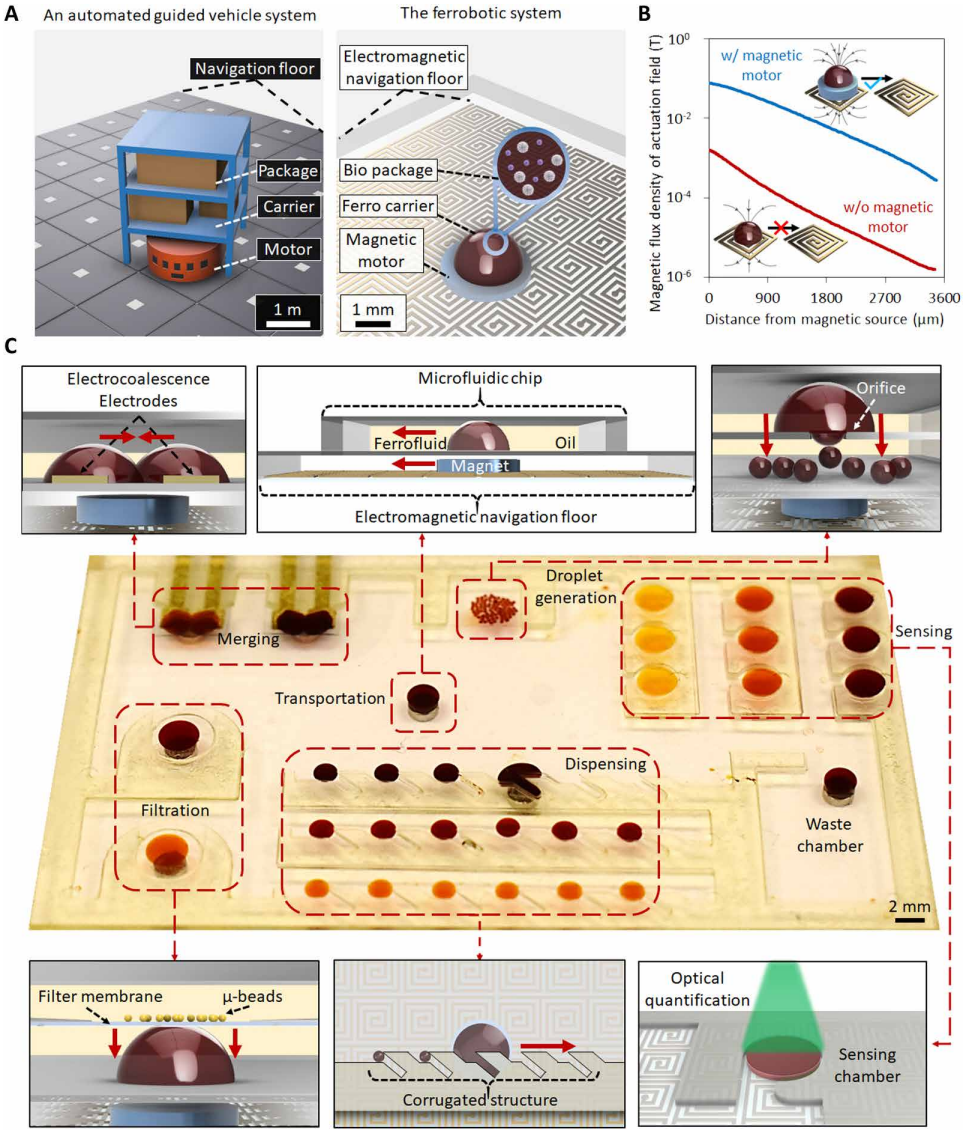

Fig. 1. Overview of ferrobotic system concept and mechanism. (**A**) An analogy: Mobility and automation in an AGV system and the devised ferrobotic system. (**B**) Simulation results depicting the amplification of the actuation capability with the magnetic motor (the *x* axis is the vertical distance from the center of the magnetic source). (**C**) Optical image of a representative multifunctional ferrobotic system capable of performing diverse operations, including droplet package transportation, merging, generation, filtration, dispensing, and sensing. Rendered images of the droplets are for illustration purposes only (droplets can form hemisphere or disk-like shapes depending on the channel geometry).

we specifically applied this system to execute a set of cross-collaborative and diverse operations toward the quantification of active matrix metallopeptidases (MMPs; a biomarker for cancer malignancy and inflammation) in human plasma (*22*–*24*), where its reconfigurable functionality and teamwork capability converged to implement a fully automated assay.

RESULTS

Amplified addressable EM actuation

By using the EM coil matrix as the addressable actuator and the millimeter-scale permanent magnet as the magnetic field actuation amplifier, we could realize robust ferrobotic fluid operations within a compact footprint. As seen in the magnetic field simulation results, illustrated in Fig. 1B and fig. S1, the incorporated permanent magnet amplifies the actuation magnetic field by approximately two orders of magnitude (generated from passing a 0.2-A DC current through the EM coil). In this way, high-force actuation of relatively dilute magnetic solutions and/or smaller fluid volumes was achieved, rendering robust fluid transportation. Fluid transportation is the ferrobotic system's core functionality, where an encapsulated package within the ferrofluidic carrier can be directed by the sequential activation of the EM coils along a desired route on the navigation floor.

The navigation floor was fabricated on a multilayer printed circuit board (PCB), which at its core is composed of a matrix of 32 by 32 EM coils, where each element is realized as a three-layered spiral structure (fig. S1). The multilayer implementation allows the proportional increase of the localized EM induction capability of each element for ferrobot attraction. To activate these elements in an addressable manner, we incorporated two integrated circuit (IC) switches in the PCB for row and column selection (Fig. 2, A and B), which are connected to external power sources and controlled by a microcontroller unit (MCU). Depending on the task at hand and by programming at the MCU level, these coils can be sequentially and/or simultaneously activated to engineer the desired paths for a single or multiple ferrobot(s). To illustrate this feature, we programmed the MCU to navigate single ferrobots through U-, C-, L-, and A-like routes (Fig. 2C and movie S1), as well as four ferrobots to simultaneously trace the perimeter of a square-like route (fig. S2). In all scenarios, the ferrobots successfully carried their designated loads.

These traits, together with the reconfigurability of the ferrobotic system, can be exploited to integrate passive and active functional components to implement advanced and diverse microfluidic operations (e.g., droplet dispensing, generation, merging, and filtering) besides basic transportation operations (Fig. 1C). Depending on the objective at hand, a set of these operations can be combined within a disposable microfluidic architecture to deliver versatile system-level microfluidic functionalities.

This high degree of robustness and the individual addressability of ferrobots can be in turn leveraged to deploy a network of ferrobots that carry out generalizable cross-collaborative objectives, centering on microfluidic logistics, such as fluidic package sorting. To illustrate the utility of the ferrobotic system in diverse application spaces,

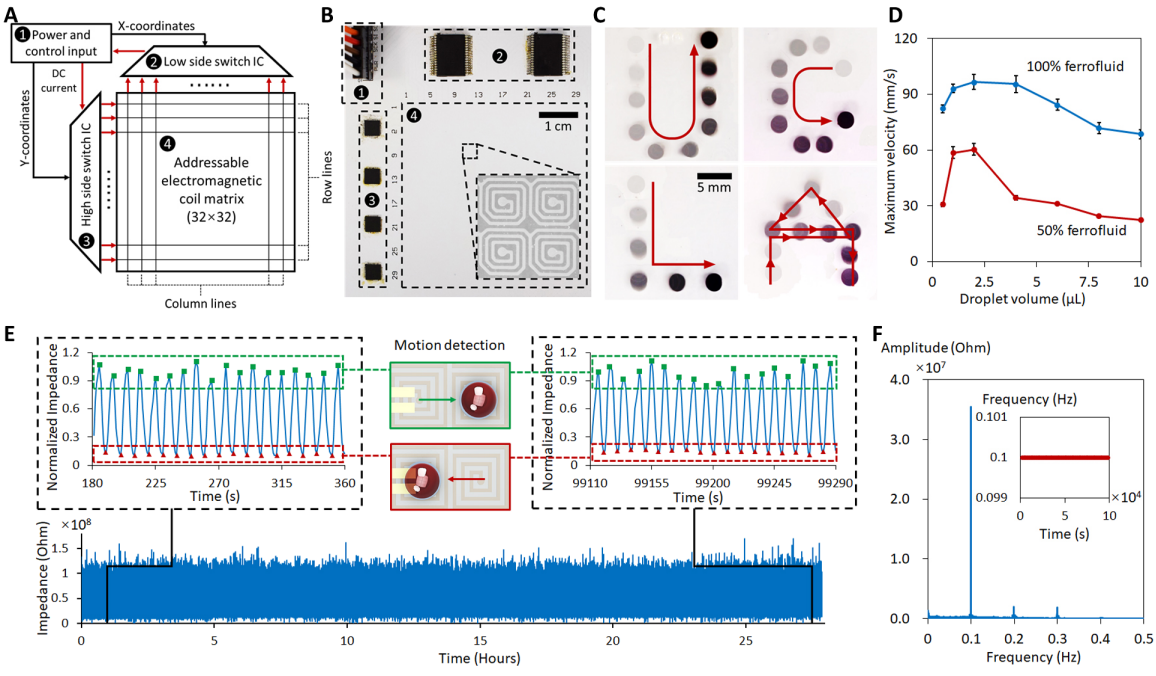

Fig. 2. Design and characterization of the navigation floor for package transportation. (**A**) Schematic diagram of the control circuitry. (**B**) Optical image of the implemented control circuitry and the navigation floor with the close-up view of four neighboring EM coils. (**C**) Overlaid sequential images (derived from video frames) visualize the commuted path of the ferrobot (programmed with different navigation plans; the durations for commuting "U," "C," "L," and "A" paths were correspondingly 1.4, 1.4, 0.7, and 2.3 s). (**D**) Characterization of the maximum transportation velocity for two different ferrofluid concentrations. Error bars, SE ($n = 3$). (**E**) Characterization of the oscillatory transportation of a package with a ferrobot (sensed with an impedance sensing electrode pair) to evaluate the robustness of the ferrobotic actuation (performed for >24 hours). (**F**) FFT analysis of the oscillatory profile measured by the impedance sensing electrodes in part (E). Inset shows variation of the fundamental frequency of the 2000-s segmented time windows, depicting near-zero variation.

As shown in Fig. 2D and fig. S3, with the devised approach, maximum droplet transportation velocities on the order of 10 cm/s could be achieved. The maximum velocity of the droplet initially increased along with its size, showing the dominance of the driving magnetic force on relatively small droplets. The following decrease in maximum velocity illustrates the increased dominance of frictional forces beyond a certain droplet size (for an expanded discussion on this topic, please refer to Supplementary Materials). The same trend was observed for a more diluted ferrofluid concentration (50% dilution by volume, also shown in Fig. 2D). Here, the droplet volume characterization range was chosen on the basis of the envisioned microfluidic droplet applications (e.g., the MMP assay).

The contactless aspect of the actuation mechanism (i.e., no ferrobotic surface interaction with the package or the surrounding fluid) inherently renders it repeatable and durable, in contrast with contact-based EWOD actuation that is susceptible to surface degradation (*16*, *17*, *25*, *26*). To demonstrate the durability of our ferrobotic system, we performed an illustrative continuous characterization experiment, which involved a 10,000 cycle automated oscillatory transport (frequency, 0.1 Hz) of a package over a duration of >24 hours (Fig. 2E). Specifically, the ferrobot was programmed to automatically move in and out of contact with an impedance sensing electrode pair (fig. S4A) patterned on the substrate of a microfluidic chip. The electrodes were used to continuously track the entrance/departure of the package through monitoring the impedance signal change (correspondingly leading to an increased/decreased measured impedance, annotated in green/red, Fig. 2E). Fast Fourier transform (FFT) analysis of the continuously recorded data (Fig. 2F) yielded an output fundamental frequency of 0.100 Hz, which matches the input actuation frequency at the MCU level. Furthermore, the detailed FFT analysis of the 2000-s segmented time windows yielded less than 0.01% variation in the motion frequency of the package. We also performed oscillatory droplet transport experiments at 1 Hz with water- and plasma-based droplets (more than 1000 cycles). The FFT analysis, shown in fig. S4 (B and C), indicates that repeatable oscillatory motions were achieved for both droplet samples. Beyond ~10 Hz, the droplet cannot be effectively manipulated because this leads to a velocity that exceeds the maximum velocity threshold.

Functional components for advanced operations: Droplet dispensing, generation, merging, and filtration

The high-strength and contactless aspects of the devised actuation mechanism can be exploited to conveniently interface the loaded package with different passive and active peripheral components and microfluidic structures in all three spatial dimensions, thus enabling operations of interest in a reconfigurable manner. For example, by carrying the package against a corrugated microfluidic structure formed in the *x-y* plane, droplet dispensing was achieved. Moreover, by delivering the droplet package within a multilayered chamber and through vertical interconnect access (VIA) and membranes along a *z* axis, droplet generation and filtering can be realized. Furthermore, without causing physical/field interference, droplets can be delivered to active electrofluidic interfaces to render complementary actuation mechanisms such as electrocoalescence for droplet merging.

Droplet dispensing is a precise liquid-handling capability that is useful for applications such as drug discovery, quantitative biology,

and chemical analysis (*27*, *28*). To implement the dispensing of uniformly sized droplets with the ferrobotic system, we used a microfluidic architecture with a corrugated wall structure. As demonstrated in Fig. 3A, a "parent" droplet package was guided by a ferrobot underneath the microfluidic chip. When it was transported along the corrugated structure, smaller "child" droplets were dispensed. As shown in Fig. 3B and movie S2, the parent droplet started moving along the corrugated wall at $t = 0$ s. After the droplet passed the corrugated structure at $t = 1$ s due to geometric pinching, a small volume of the droplet broke away from the parent and entered the structure. The corrugated structure can be extended into an array format to dispense multiple droplets. As shown in the final step of Fig. 3B, three homogenous droplets (1.63 ± 0.09 μl) were dispensed. To study the level of control that our system has on the dispensed droplet sizes, we designed and tested various corrugated-opening widths. The results show that by increasing the corrugated-opening width, the dispensed droplet volume could be modulated from 0.5 to 4 μl (Fig. 3C). The same trend was observed for diluted ferrofluid concentrations (10 and 50% dilutions by volume; fig. S5). If larger dispensed droplet volumes are needed, then a larger magnet in addition to an enlarged corrugated-opening width may be required.

Furthermore, higher throughput and smaller volume droplet generation can be realized by incorporating an orifice-like VIA connecting neighboring layers in a multilayer microfluidic architecture. As schematically illustrated in Fig. 3D, when the parent droplet is guided through the upper layer to the top of the orifice, it is attracted toward the lower layer by the vertically exerted magnetic force from the ferrobot. Every time a critical volume of the droplet passes the orifice, it breaks off into a child droplet. As shown in Fig. 3E and movie S3, the following sequential events occur: (i) the transport of the parent droplet (in the upper layer) to an orifice; (ii) the positioning of the parent droplet on the orifice to generate child droplets; and (iii) the departure of the parent droplet, leaving behind the generated child droplets (in the lower layer). By adjusting the width of the junction orifice, the droplet volume (~10 to 125 nl) and the generation rate can be tuned (Fig. 3F and fig. S6). Such nanoliter-generated droplets can also be further manipulated by the ferrobot (fig. S7).

Microfluidic filtration is one of the key sample processing procedures required for applications such as cell separation (*29*, *30*). Here, by incorporating a membrane between the two layers of the microfluidic device, size-based filtration was realized. As schematically shown in Fig. 3G, the contactless magnetic force exerted by the ferrobot causes the droplet to be pulled through the filter to the lower layer, leaving behind particles that are too large to pass through. Specifically, here, a membrane with a size cutoff of 10 μm was used to filter out μ-beads with a diameter of 25 μm. To quantify the filtration capability, we optically imaged the ferrofluid droplet before and after the filtration procedure. As can be seen from Fig. 3H, 25-μm μ-beads can be observed in the droplet before filtration and are subsequently filtered out, as evident from the postfiltration optical analysis results (three trials; Fig. 3I).

Droplet merging allows for timed and metered addition of reagents and can play

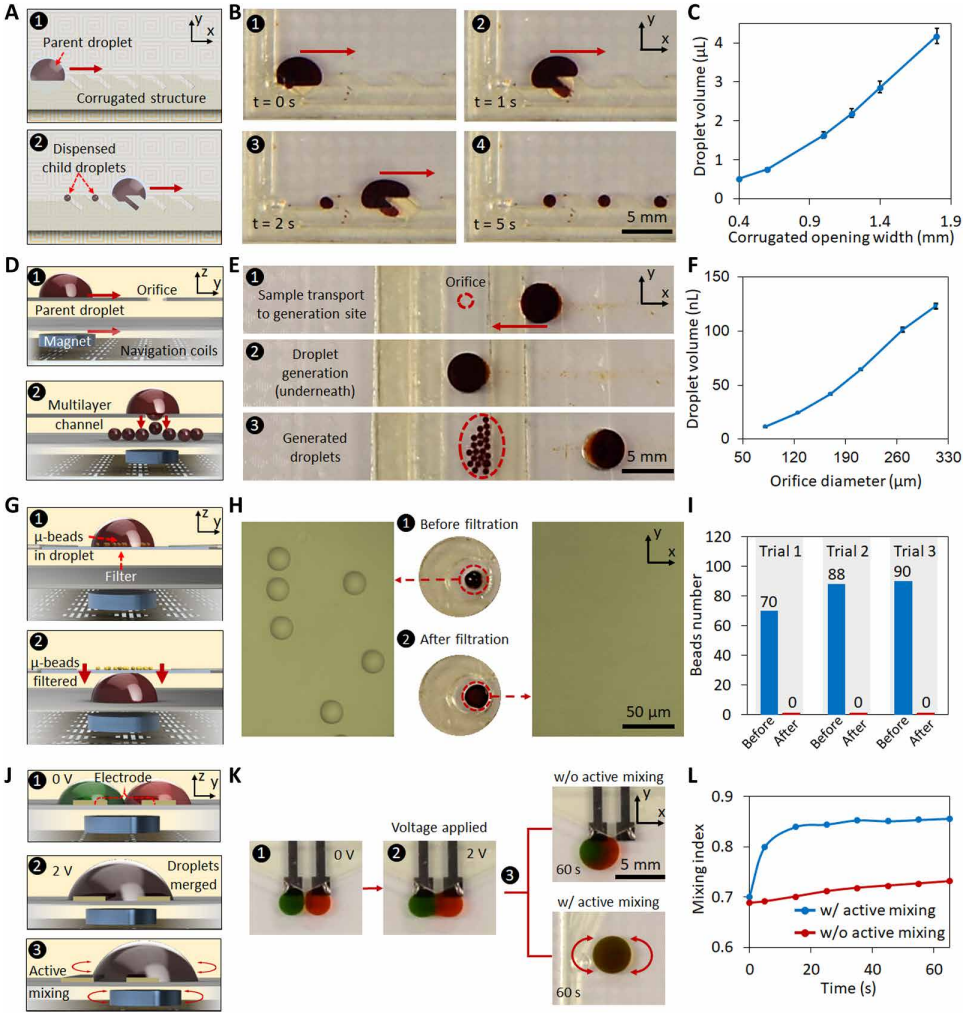

Fig. 3. Demonstration and characterization of advanced operations achieved with functional components. (**A**) Schematic illustration of the droplet dispensing mechanism involving the transportation of the package against a corrugated microfluidic wall. (**B**) Sequential optical images of the droplet dispensing process. (**C**) Characterization of the dispensed droplets' size for different corrugated opening widths. Error bars, SE ($n = 10$). (**D**) Schematic illustration of the droplet generation process involving the droplet transportation to a VIA-like orifice. (**E**) Sequential optical images of the droplet generation process. (**F**) Characterization of the generated droplets' volume for different orifice diameters. Error bars, SE ($n = 20$). (**G**) Schematic illustration of the filtration mechanism. (**H**) Optical image of the solution sample before and after filtration. (**I**) Bead counts before and after filtration (three trials). (**J**) Schematic illustration of droplet merging and mixing mechanisms. (**K**) Optical images to visualize the droplet merging (upon applying 2 V) and mixing process (with and without active mixing). (**L**) Comparison of the progressive mixing index for the two cases of with and without active mixing.

a critical role in performing droplet-based biological assays that aim to measure DNA/RNA, protein, and cell properties in samples (*31*–*35*). Here, to achieve the merging of droplets in the ferrobotic system, we leveraged electrocoalescence as a complementary actuation mechanism, which is noninterfering with the contactless ferrobotic actuation (Fig. 3J). Accordingly, electrocoalescence is realized by applying 2 V across a pair of gold electrodes (2 mm by 2 mm, spaced 1 mm apart, patterned on the substrate of the microfluidic device). Figure 3K and movie S4 show that upon applying 2 V, two droplets delivered in the vicinity of the electrodes coalesce. To achieve homogeneous and evenly distributed droplet contents after merging, chaotic fluid motion within the merged droplet can be induced by actuating neighboring EM coils with a frequency of 10 Hz in a cyclic fashion, resulting in an oscillatory motion of the ferrobot within the confines of the coil's coordinates. This cyclic motion creates folding flows in alternating directions to effectively render mixing. Figure 3K visually demonstrates the substantial effect of the devised active mixing on shortening the time required to achieve homogeneity in a merged droplet. To quantify this effect, we performed optical analysis on the merged red/green droplet by defining a mixing index (see the "Droplet merging" section in Materials and Methods.). The results are illustrated in Fig. 3L, demonstrating that a near-homogenous profile is achieved within ~15 s using active mixing, which is substantially shorter than without active mixing.

Efficient achievement of objectives with a cross-collaborative network of ferrobots

The robustness and addressability of the ferrobotic system can be leveraged to deploy fleets of ferrobots to dynamically accomplish collaborative tasks in parallel toward the more efficient achievement of a common objective. Here, as an example, a package-sorting mission is assigned to the ferrobotic system, where the objective is to sort randomly sequenced packages into a sorted sequence of increasing droplet volumes. Figure 4A illustrates the system-level view of the sorting procedure, which includes (i) loading of multiple packages of various sizes into the ferrobotic system with random relative positions; (ii) top-view image acquisition of the packages on the navigation floor to identify the package sizes and positions; (iii) computationally deriving the navigation plan to formulate the detailed tasks for the ferrobots in accordance to the "merge sort" algorithm (*36*) and the acquired size and position information; and (iv) communicating the corresponding assigned tasks for each of the ferrobots with the aid of the on-board microcontroller to achieve the overarching sorting objective. To particularly demonstrate the degree of efficiency that can be attained when deploying a cross-collaborative network of ferrobots, we compared the n-package sorting performance achieved by a team of n ferrobots against that achieved by a single ferrobot on the basis of the completion time (as detailed in Fig. 4, B and C, for an illustrative case of $n = 8$).

When only one ferrobot is used for sorting, it is responsible for the delivery of all the packages by itself. At each state (defined as the period during which the available ferrobot starts and finishes one round of package delivery), only one package can be moved to its target location. To quantitatively characterize the sorting efficiency, we defined a "unit step," which equals to the distance between two navigation coils, to measure the distance that the ferrobots will move. For example, referring to Fig. 4B, at state 1, the ferrobot moves eight unit steps (two vertical steps and six horizontal steps) to deliver package 2 ("P2") from position 8 to position 2. Because only one ferrobot is performing the task, the "temporal steps" (number of steps, which determine the maximum time elapsed over the course of a state) required to complete sorting are equal to the total unit steps moved by the single ferrobot. In the example shown, it takes the single ferrobot a total of 40 temporal steps to meet the sorting objective.

When multiple ferrobots are deployed (Fig. 4C), each ferrobot is charged with moving one package, and they can move in parallel with other ferrobots during the same state (following the computationally derived navigation plan in accordance with the "merge sort" algorithm; fig. S8A). The corresponding experiment is visualized in Fig. 4C (right) and movie S5. In this scenario, the number of temporal steps for each state is determined by the maximum steps taken by a ferrobot within the team because the ferrobots are delivering packages in parallel. For example, referring to Fig. 4C, in state 2, among eight ferrobots, one ferrobot moves zero steps, two ferrobots move three steps, and five ferrobots move four steps, yielding four temporal steps for that state. The total number of temporal steps to achieve the sorting objective is also equal to the sum of temporal steps for each state, which is 13 for the illustrated example. By comparison, for this illustrative example, sorting using multiple ferrobots results in about 300% increased efficiency as compared with the single ferrobot case. This degree of improvement achieved due to the deployment of a cross-collaborative network of ferrobots will be even higher for the cases requiring sorting of a larger number of packages (i.e., larger n). That is because the complexity of the mission at hand for the case of a single ferrobot increases as $O(n^2)$, whereas for the case of multiple ferrobots, it increases linearly [i.e., $O(n)$]. To reinforce this point, as shown in Fig. 4D, we derived the total temporal unit steps for the cases of $n = 2$, 4, 8, and 16, based on statistical averaging of all the possible permutations (consistent with the trend observed when simulating 10,000 randomly generated sequences of n packages; fig. S8B). Together, the results presented within the framework of this generalizable objective illustrate the utility of the deployment of a network of ferrobots to achieve the objective at hand efficiently and the suitability of the ferrobotic system for microfluidic logistics.

Application of the ferrobotic system to implement a pipelined and automated bioassay

Leveraging the demonstrated capability of the ferrobotic system to deliver advanced and cross-collaborative operations, we implemented a pipelined and automated bioassay equipped with a dynamic self-calibration mechanism as an example utility of the presented technology in diverse application spaces centering on microfluidic logistics. Accordingly, the ferrobotic logistics were adapted to quantify MMP concentrations in human plasma. MMPs are biomarkers extensively studied and reported as immunological indicators, wherein the elevation of plasma MMP concentration is associated with physiological and pathological processes such as cancer metastasis (*22*, *23*, *37*), sepsis onset (*38*–*40*), immune activation (*24*, *41*), and wound healing (*42*, *43*).

Figure 5A illustrates the workflow of the MMP assay, which is based on the fluorescent quantification of the enzymatic activity of MMPs from a test sample (introduced into the input well) and the calibrator samples indicated by the intensity of fluorescent signals. To realize an automatic self-calibration mechanism, we used preloaded source samples (introduced at the source well array, with known concentrations of the MMP collagenase) for the construction of calibrator samples in situ, providing optional flexibility to dynamically

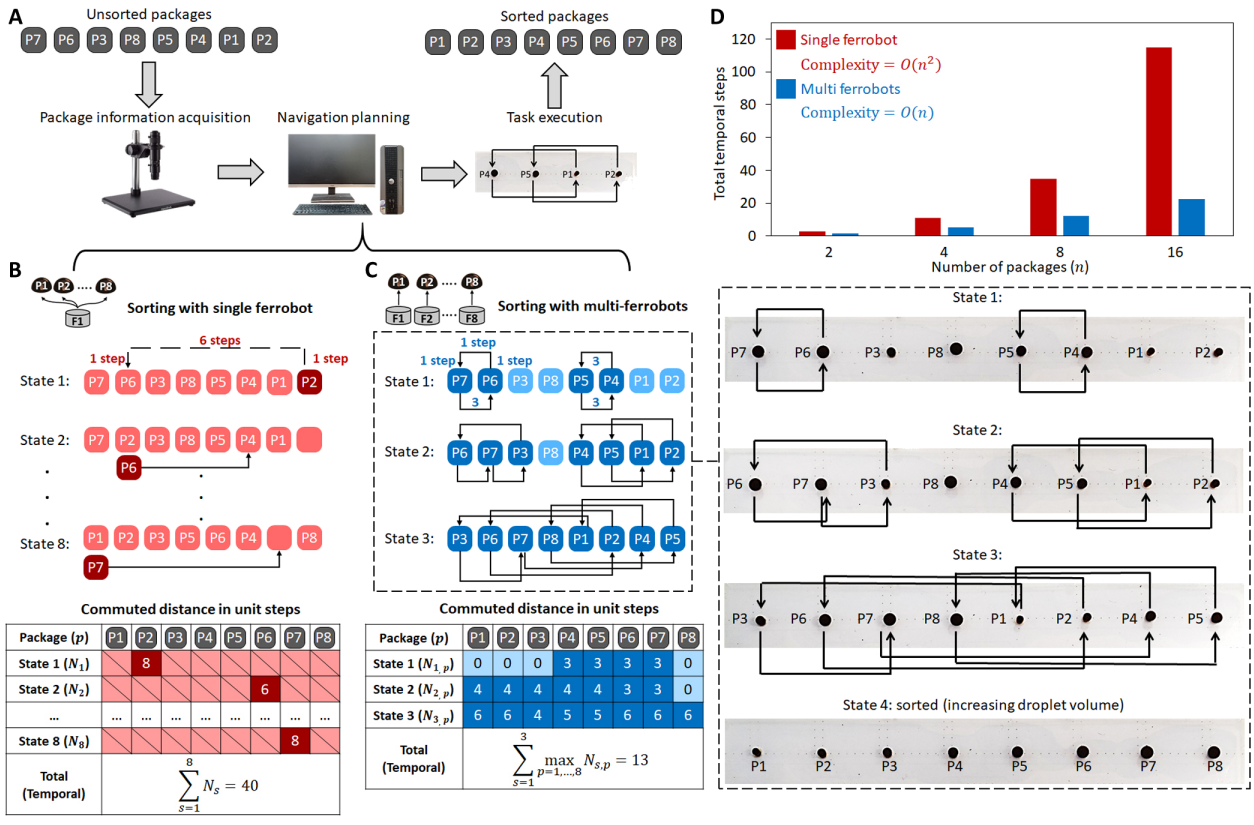

Fig. 4. Efficient package sorting with a cross-collaborative network of ferrobots. (**A**) System-level view of the sorting procedure. (**B** and **C**) Comparison of the sorting efficiency achieved by (B) a single ferrobot and (C) eight ferrobots tasked with sorting a random sequence of eight packages. State-by-state transitions for both scenarios are illustrated, and the left table details the commuted distance of each ferrobot. The snapshots from the sorting experiment performed with eight ferrobots are shown on the right (captured at the end of each state). (**D**) The total temporal unit steps required for sorting 2, 4, 8, and 16 packages (based on statistical averaging of all the possible permutations).

construct new calibrator concentrations (e.g., [C_2] in Fig. 5A). To facilitate optical readout, we preloaded a fluorescence resonance energy transfer (FRET)–based MMP substrate in the calibration well array and the output well (designated for test sample analysis). The self-calibration capability of the assay establishes a standard curve in situ and concurrently with the testing assay, which is particularly useful for mitigating systematic error typically associated with fluorescence spectrometry and ensuring the accuracy of the measurements (*44*).

The ferrobotic system was programmed to implement the steps of the automated assay within a microfluidic architecture, including (i) sample collection, (ii) dispensing (to ensure uniform sample volume), (iii) delivery, and (iv) merging (with the aid of an electrocoalescence electrode pair) and mixing for sensing (Fig. 5B). Specifically, three ferrobots (F_1, F_2, and F_3) were used to carry out the required tasks in a pipelined manner. The overview of the navigation plans of the three ferrobots is shown in Fig. 5C. In this regard, ferrobot F_1 is in charge of collecting and dispensing the source and test samples into smaller uniform droplets. Ferrobot F_2 is responsible for delivering the dispensed droplets to the designated detection wells, and ferrobot F_3 is tasked with removing the dispensed droplet residues to the waste chamber. The detailed timeline of the task sequence executed by each ferrobot in coordination with the other two ferrobots, along with representative snapshots of the navigation floor status, are illustrated in Fig. 5 (C and D) and movie S6.

Upon delivering the dispensed calibrator/test sample droplets to the calibration well array/output well, the electrocoalescence electrode pair (a single pair patterned across all the detection wells) is activated, merging the delivered droplets with the preloaded MMP substrate within each well all at once. To achieve a homogenous mixture after merging, ferrobot F_2 can induce a chaotic internal flow. Upon merging and mixing of the samples with MMP substrate, enzymatic reactions (Fig. 5E) effectively commence at the same time, resulting in the generation of fluorescent signal proportional to the respective MMP content in a well. The fluorescent signals are quantitively analyzed by fluorescence microscopy. The linearity of the fluorescent signals with the MMP content of a sample was validated by spiking collagenase in a phosphate-buffered saline (PBS) buffer at different levels and reading out fluorescence after a 10-min incubation (fig. S9). To evaluate the analytical accuracy of the ferrobotic assay for measuring the MMP content in human plasma, we used four calibrator samples with collagenase concentrations of 0.003, 0.006, 0.009, or 0.012 Wünsch U/ml to determine the MMP concentration of a test sample (human plasma spiked with MMP at a collagenase concentration of 0.008 U/ml). As illustrated in Fig. 5F, by referring to the real-time standard curve generated by the calibrator samples, the test sample MMP content was measured to be 0.0078 ± 0.0005 U/ml (based on 95% confidence interval). To further evaluate the analytical performance of the ferrobotic assay, we analyzed four additional test samples by the ferrobotic system and by a technician using manual pipetting

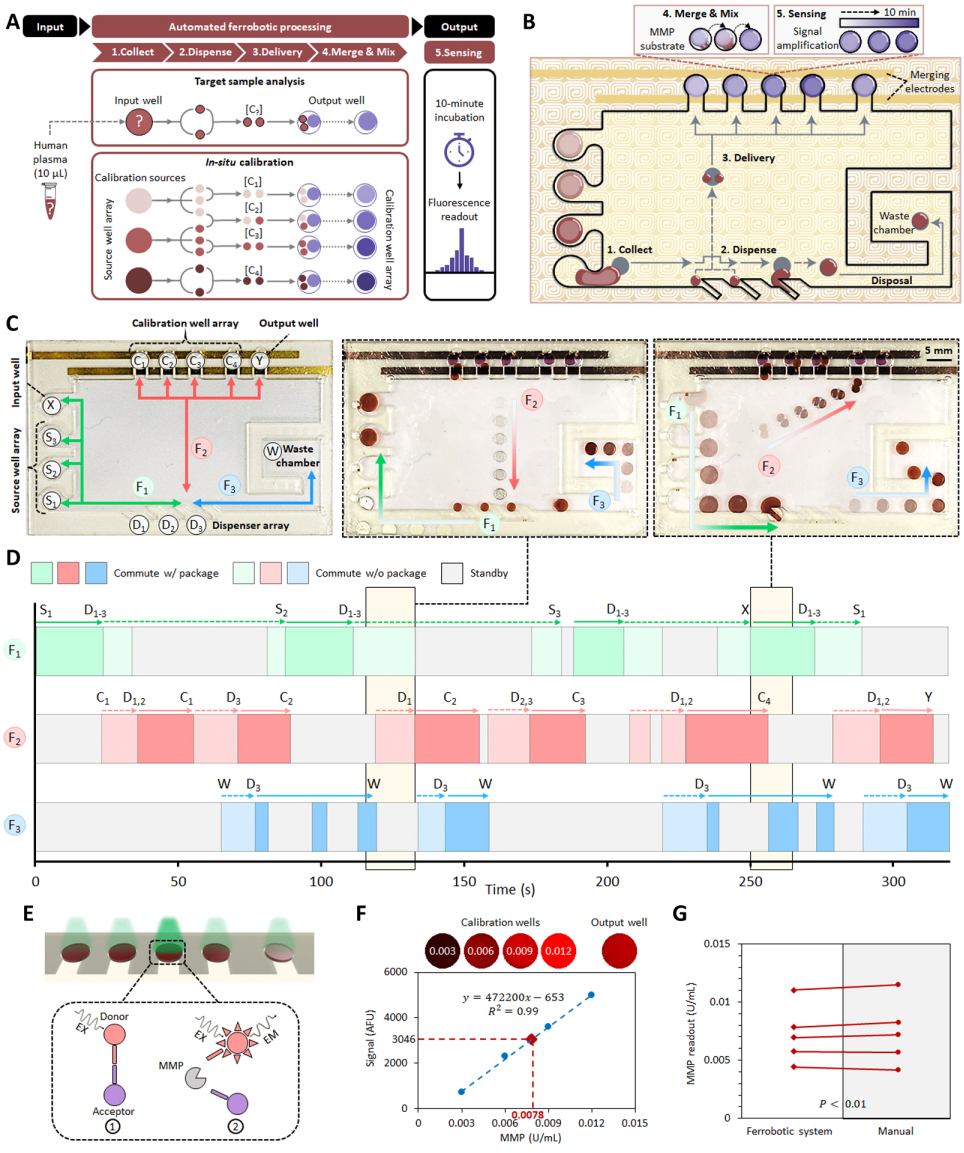

Fig. 5. Pipelined and automated MMP assay performed by the ferrobotic system. (**A**) General workflow of the MMP assay equipped with a dynamic self-calibration mechanism. (**B**) Illustration of the ferrobotic tasks in relation to the navigation floor over the processing of a representative sample (performed by three ferrobots). (**C**) Overview of the navigation plans of the three deployed ferrobots (F_1, F_2, and F_3) with annotated locations of interest. (**D**) The detailed timeline of the ferrobots' status (commuting with/without package, standby), with annotated locations of interest. Overlaid sequential video frames illustrating the status at two representative stages. (**E**) Illustration of the FRET pair from the MMP substrate cleaved by the MMPs present in the sample to yield a fluorescent product that is no longer quenched. (**F**) The fluorescent readouts [arbitrary fluorescence unit (AFU)] from the calibration and output wells after automated ferrobotic processing and 10 min of incubation. The concentration of MMP in the test sample is estimated with the aid of a real-time calibration standard curve generated from the four calibrator samples [0.0078 U/ml (estimated) versus 0.008 U/ml (expected)]. (**G**) Estimated MMP concentrations in five tested human plasma samples (performed by the ferrobotic system and manually by a technician; $P < 0.01$).

steps and a plate reader (*45*). As shown in Fig. 5G, the readouts obtained from the ferrobotic system closely matched those analyzed using standard manual analysis ($P < 0.01$), which, in turn, illustrates the successful execution of all ferrobotic instructions with a high degree of robustness and precision. This pipelined assay exemplifies the capacity of the ferrobotic system to perform highly quantitative biochemical processes with a high level of integration and automation.

DISCUSSION

Inspired by the degrees of freedom achieved by the emergence of AGV robotic systems in terms of mobility and automation, here we introduced and experimentally demonstrated the concept of a ferrobotic system. Accordingly, an amplified addressable EM actuation mechanism is devised for robotic guidance. The contactless (i.e., no ferrobotic contact with the package or the surrounding fluid) and high-strength actuation mechanism inherently renders it rapid (10 cm/s), repeatable (>10,000 cycles), and robust (>24 hours). These traits, together with the reconfigurability of the system, enabled the implementation of advanced and diverse operations through the integration of passive and active functional components. To this end, we designed and characterized droplet microfluidic operations—including dispensing, generation, merging, and filtering—where the results indicated minimal undesired operational performance deviation. Furthermore, we demonstrated the significantly elevated efficiency of the ferrobotic system for microfluidic logistics applications by deploying a network of cross-collaborative ferrobots to deliver an illustrative and generalizable package sorting objective. To showcase an application where logistics of sample dosing, merging, and mixing are required, we leveraged the advanced and cross-collaborative ferrobotic operations to achieve a pipelined and automated bioassay for the quantification of MMPs in human plasma.

Collectively, our characterization results demonstrate precise, repeatable, durable, and cross-collaborative ferrobotic operations in versatile settings. Although these operations were realized with a 32-by-32 addressable navigation floor, the scale of the ferrobotic operations can be expanded by simply adopting a larger navigation floor (requiring minimal reconfiguration of the PCB, specifically, increasing the number of EM coils). In that regard, augmentation with image or electrical ferrobot/droplet positioning sensing capabilities within the ferrobotic system will allow for the implementation of a feedback control process as a corrective measure to ensure the robustness of desired large-scale operations. Furthermore, the optical readout of the assay is currently performed using a benchtop fluorescence microscope. Further automation and integrated sample-to-answer solutions, especially in point-of-care settings, would benefit from integrated low-cost readers leveraging

consumer electronic devices (*46*). Alternatively, other assays could be read using electrochemical sensors, which can be integrated onto the platform in a similar manner as the electrodes used for electrocoalescence. Exploiting the ferrofluid biocompatibility (*47*, *48*), fluorescence and electrochemical assays can be adapted for applications centering on cell and nucleic acid analysis (*27*).

On a broader level, adaptation of the ferrobotic system for translational applications necessitates future and convergent designated efforts in microscopic and macroscopic domains toward establishing a generalizable design space for the ferrobotic system. Microfluidic physics-focused efforts are required to comprehensively model the underlying ferrobotic actuation mechanism and understand its limitations in relation to relevant forces, scaling of dimensions (including magnet-, droplet-, and microfluidic structure dimensions), fluidic properties, and other design parameters. Furthermore, macroscopically, dynamic navigation planning algorithms are required to optimize the performance of the cross-collaborative ferrobots toward the delivery of the required objective(s) and in the presence of operational constraints (such as a ferrobotic "safety distance"). To this end, readily developed models from the AGV community aiming to address issues such as layout challenges, fleet management, speed/movement limitations, and optimization functions can be adapted and applied within the framework of the ferrobotic system.

The versatility, scalability, and reconfigurability of the devised ferrobotic system allow for its adaptation to perform diverse and massively parallelized and sequential microfluidic operations relevant to diverse application spaces including point-of-care diagnostics, -omics, drug development, and chemical/material synthesis. By capitalizing on the high degree of automation that can be achieved by the presented technology, large datasets can be generated to unravel complex biological and chemical processes, seeding the transformation of the biotechnology and pharmaceutical industries and mirroring the impact of the AGV robotic systems on their respective industries.

MATERIALS AND METHODS

Materials for the ferrobotic system

The ferrofluid used in this work refers to ferumoxytol, a U.S. Food and Drug Administration–approved intravenous iron preparation also referred to as Ferraheme (AMAG Pharmaceuticals, MA, USA). Rare earth permanent magnets (D101, 0.8 mm in thickness and 2.54 mm in diameter) were purchased from K&J Magnetics (PA, USA). All microfluidic devices were filled with fluorinated oil (Novec 7500 Engineered Fluid, 3M, MN, USA) containing 0.1% biocompatible surfactant (Pico-Surf 1, Sphere Fluidics, NJ, USA). The design and fabrication of the microfluidic devices and the EM navigation floor are described in detail below.

EM navigation floor circuit design

The EM navigation floor on the PCB comprised an active matrix array of 32 EM coil elements by 32 EM coil elements. Each element had a three-turn coil with a size of 1.5 mm by 1.5 mm stacked on three layers. Adjacent coils were separated by a gap of 0.1 mm, together, giving a total active area of the navigation floor of 51 mm by 51 mm.

Each coil element can be activated when powered by a 0.2-A current, generating a localized magnetic force that attracted the magnetic motor. The specific coil selection was achieved by programming power switch ICs, including MAX14662 (Maxim Integrated, CA, USA) for row selection and MC33996 (NXP Semiconductors, Netherlands) for column selection in the navigation floor. The target EM coil was selectively actuated when the corresponding row and column lines of its coordinate were activated by switch ICs. Switch ICs were linked by serial peripheral interface (SPI) wires to Arduino Nano, which communicated with a computer through serial communication. Target coordinates preprogrammed or sent from the user interface in the computer were translated to SPI commands by the MCU and then transmitted to switch ICs for addressable activation of the EM coils.

The navigation floor was powered by an external power supply (Keithley 2230-30-1, Tektronix, OR, USA). A DC current source was used for EM coil activation, and the total current I followed the equation: $I = 0.2\ A \times N$ (N is the number of activated coils).

Microfluidic device fabrication

Similar to previous work (*49*), functional microfluidic devices were created by assembling several layers of double-sided tape (170 μm thick, 9474LE 300LSE, 3M, MN, USA) and transparent polyethylene terephthalate (PET) film sheets (416-T, MG Chemicals, BC, Canada). Microchannels and VIAs (i.e., holes vertically passing through the sheets) were created by laser cutting (VLS 2.30, Universal Laser System, AZ, USA) two-dimensional (2D) patterns within the tape and the PET substrates. Through the alignment of vertical VIAs and microchannels, fluidic connections in both horizontal and vertical directions were achieved, rendering functional 3D microfluidic structures. In some devices, PET sheets were selectively patterned with gold electrodes before assembly. The electrodes were fabricated on PET substrates by photolithography using positive photoresist (AZ5214E, MicroChemicals, Germany), followed by the evaporation of 20 nm of Cr and 100 nm of Au. After deposition, a lift-off step was performed in acetone.

EM field simulation

To investigate and model the effect of an intermediary permanent magnet on amplification of the actuation magnetic field, we used finite element analysis (COMSOL Multiphysics 5.2, MA, USA) to perform EM simulations. In the simulation setup, magnetic and electric field physics were used in an air environment. The simulation used the same EM coil and permanent magnet dimensions as the experimental setup (fig. S1). The magnetization of the permanent magnet was set according to the product description (278.9 kA/m in axial direction), and the intensity of actuation for the DC current was set as 0.2 A. The magnetic flux density profile was generated on the x-z plane.

Maximum transportation velocity characterization

A microfluidic device with a 40-mm–by 40-mm–by 1.5-mm inner chamber was fabricated, assembled, and filled with oil. The device was placed 2 mm above the navigation floor. A magnetic motor was placed on top of the navigation floor and below the microfluidic device.

Ferrofluid droplets with volume gradients of 0.5 to 10 μl (0.5, 1, 2, 4, 6, 8, and 10 μl) and two different concentrations (100 and 50% ferumoxytol dilution in deionized water) were loaded in the microfluidic chamber. These droplets moved along with the ferrobot, which was sequentially guided by the EM coils actuation in one row from left (y = 1) to right (y = 32). The velocity of the ferrobot was

controlled by adjusting the time interval between activating two adjacent coils. If the ferrofluid droplet followed the magnetic motor to the end successfully, then the velocity of the magnet would increase by shortening the actuation time interval (by 1 ms) in the next round until the droplet failed to follow the magnet.

Characterization of the long-term and oscillatory ferrobotic transportation

A microfluidic device with a 20-mm by 20-mm by 0.7-mm chamber was fabricated and assembled, with a pair of gold electrodes deposited on the substrate as an impedance sensor. A 2-μl ferrofluid droplet was loaded in the oil-filled microfluidic chamber. A magnetic motor was periodically actuated to carry the droplet back and forth between two locations (0.1 Hz). In each cycle, the droplet was first carried away from the sensing electrodes, consequently raising the impedance signal, and then carried back in contact with the electrodes, causing the impedance signal to drop. These actions were repeatedly performed for more than 100,000 s to finish 10,000 cycles. The electrodes were connected to a potentiostat (CH Instrument 660E, TX, USA), and impedance (at 1 kHz) was measured between the two electrodes.

Droplet dispensing setup and procedure

Microfluidic devices (20 mm by 40 mm by 0.7 mm) with corrugated wall structure on one side were fabricated and assembled. Six devices with same corrugated opening length (3 mm) and different opening widths (0.4, 0.6, 1.0, 1.2, 1.4, and 1.8 mm) were tested. A 10-μl parent ferrofluid droplet was loaded in each microfluidic devices filled with oil. During the experiment, the parent ferrofluid droplets were transported along the corrugated structures, leaving dispensed droplets in corrugated openings. The sizes of the five dispensed droplets were measured through image analysis.

Droplet generation setup and procedure

Multilayer microfluidic devices with a vertical orifice junction in the middle PET layer (800 μm above the bottom surface) were fabricated and assembled. Different vertical orifices were fabricated by laser cutting and measured under the microscope, resulting in diameters from 80 to 310 μm. A 4-μl parent ferrofluid droplet was loaded in the upper layer of the microfluidic device. During the experiment, the droplet was transported to the vertical orifice junction by a ferrobot and stayed static for 4 s. The diameters of the generated small droplets were measured under a microscope, and volumes were calculated on the basis of the equation of a sphere. The number of droplets was counted for generation rate characterization.

Microfluidic sample filtration setup and procedure

A microfluidic device with a circular polycarbonate membrane incorporated in the top layer (PCTF10047100, Sterlitech, WA, USA) was fabricated and assembled. Monodisperse polystyrene microspheres (25-μm diameter; 24811-2, Polybead, PA, USA) were added in the ferrofluid solution for the experimental characterization of filtration. The sample was diluted from an initial concentration (5.69×10^6 beads/ml) to 8×10^4 beads/ml by ferrofluid. At the start, 1 μl of the bead-containing sample was dropped on the filter membrane. Then, the ferrobot moved to the droplet, located under the membrane region, and remained there for about 10 s until the entire droplet passed through the filter. The number of beads was counted under the microscope before and after filtration.

Droplet merging and mixing setup and procedure

A microfluidic device with patterned electrocoalescence electrodes (area of 2 mm by 2 mm, spaced 1 mm apart, thicknesses of 20 nm of Cr and 100 nm of Au) on the PET substrate was fabricated and assembled. Two 2-μl ferrofluid droplets (10% ferumoxytol solution containing either green or red food dye) were loaded in the oil-filled device. The ferrobot delivered the two droplets at the vicinity of the actuation electrode. DC voltage (2 V) was applied between the two electrodes, causing the droplets to merge. Afterward, the ferrobot either kept the droplet static (shown as "w/o active mixing condition" in Fig. 3L) or induced chaotic motion by the actuated neighboring EM coils within the confines of the coil's coordinates at a frequency of 10 Hz in a cyclic fashion (shown as "w/ active mixing condition" in Fig. 3L). A video recording was taken of the merging process, and the level of mixing was calculated through image processing as discussed below.

Mixing index calculation through image analysis

To quantify mixing efficiency, we characterized the merging of two packages with different colors (red food dye and green food dye in 2 μl of 10% ferrofluid droplet) with or without active mixing. The microfluidic region containing merged droplet was video-recorded, and the corresponding video frames were imported into a MATLAB (Mathworks, MA, USA) in [R, G, B] vector format. Image analysis was performed at droplet region. Similar to previous work (*50*), a mixing index is defined, as expressed below

$$\text{Mixing index} = 1 - \sqrt{\frac{1}{N-1}\sum_{i=1}^{N}\frac{|\mathbf{c}_i - \mathbf{c}_{\text{ave}}|^2}{|\mathbf{c}_{\text{ave}}|^2}}$$

where N, $\mathbf{c}_i$, and $\mathbf{c}_{\text{ave}}$ are the total number of pixels, the [R, G, B] values at pixel i, and the average [R, G, B] values over N pixels, respectively.

Package-sorting setup and procedure

To implement the sorting of multiple ferrofluidic packages, we fabricated a PCB navigation floor composing of an EM coil array (9 rows and 120 columns) and switch ICs. A microfluidic device with a 20-mm by 120-mm by 0.8-mm inner chamber was fabricated, assembled, and filled with oil. Eight ferrofluid droplets of different volumes (sequentially increasing from 0.5 to 4 μl) were loaded into the chamber and lined in a random order. One ferrobot was placed under each ferrofluid droplets. A top-view image of droplets was acquired and processed by a MATLAB script to identify the droplet sizes and positions, followed by the computation of a navigation plan according to the merge sort algorithm. An on-board microcontroller implemented the navigation plan, which it received through serial communication, by actuating the EM coils according to derived trajectories. The design of the navigation plan took into consideration the maintenance of an interferrobotic distance of 11 mm (seven EM coils apart) to avoid interferrobotic magnetic interference.

Implementation of the pipelined and automated bioassay with the ferrobotic system

A microfluidic device with a source well array, an input well, a dispenser array, a waste chamber, a pair of electrocoalescence electrodes (patterned across all the detection wells), a calibration well array, and an output well was fabricated and assembled as shown in Fig. 5C. Three human plasma samples, 7.2 μl each, spiked with collagenase (0.003, 0.009, and 0.012 U/ml, respectively; Collagenase/Dispase,

Sigma-Aldrich, MO, USA), were each mixed with 0.8 μl of ferrofluid and preloaded in the source well array. Four microliters of 10% (v/v) diluted MMP substrate (MMP Red substrate, AAT Bioquest, CA, USA) in PBS containing 2% (v/v) ferrofluid was preloaded into each of the calibration wells and the output well. The rest of the device was filled with oil. Eight liters of a test sample (a mixture of 0.8 μl of ferrofluid and 7.2 μl of human plasma spiked with collagenase at an arbitrary concentration) was pipetted into the input well. Thereafter, three ferrobots collaboratively performed the sample processing steps of collection, dispensing, delivery, and disposal for each source and test sample. During the sample droplet transportation, on rare occasions, miniscule fractions of the sample break free as satellite droplets, but this artifact could be ignored because the fractions constituted less than 0.5% of the original droplet volume (based on image analysis). Each calibration well or output well ended up receiving two droplets of the samples, respectively, from either the calibration source or the test sample. In situ construction of a calibrator sample was achieved through delivering two different calibration source droplets into one calibration well [e.g., in calibration well no. 2, collagenase with a concentration of 0.006 U/ml would be made by delivering one droplet with a concentration of 0.003 U/ml and another with 0.009 U/ml]. To merge the delivered droplets with the preloaded MMP substrate, we applied a voltage of 2 V across the electrocoalescence electrode pair. After 10 min of incubation, the calibration well array and the output well were imaged using a Nikon Ti-E fluorescence microscope equipped with a Photometrics Prime sCMOS camera (tetramethyl rhodamine isothiocyanate channel, 1-s exposure). Images were processed using ImageJ and MATLAB to quantify the mean fluorescence intensity in the regions of interest.

MMP quantification with a conventional well plate reader

For MMP measurements using a conventional well plate reader, we used 100 μl of calibration and test solutions (a mixture of 50 μl of human plasma spiked with collagenase of various concentrations matching the corresponding ferrobotic experiments and 50 μl of a 1% MMP substrate diluted in PBS). The measurements were performed by a BioTek Cytation 5 Imaging Reader using λ_{ex} = 540/20 nm and λ_{em} = 590/20 nm for 2 hours with lids on.

Human plasma sample

All blood samples were obtained following University of California, Los Angeles, Institutional Review Board (IRB)–approved protocol IRB no. 11-001120 and deidentified. Upon collection, blood was centrifuged using an Eppendorf 5417R Refrigerated Centrifuge, and the supernatant was frozen at −20°C in small aliquots until used.

SUPPLEMENTARY MATERIALS

robotics.sciencemag.org/cgi/content/full/5/39/eaba4411/DC1
Text
Fig. S1. EM coil geometry and magnetic field simulation.
Fig. S2. Multiferrobot transportation.
Fig. S3. Characterization of the average velocity profile of the droplet.
Fig. S4. Impedance spectrum measured by the impedance sensing electrode pair.
Fig. S5. Dispensed droplet characterization.
Fig. S6. Droplet generation characterization.
Fig. S7. Collective transportation of nanoliter droplets by a ferrobot.
Fig. S8. Merge sort algorithm and sorting performance for single versus multiferrobots.
Fig. S9. Characterization of the MMP assay.
Movie S1. Ferrobotic commute with different trajectories.
Movie S2. Ferrobotic droplet dispensing.
Movie S3. Ferrobotic droplet generation.
Movie S4. Ferrobotic droplet merging and active mixing.
Movie S5. Cross-collaborative ferrobotic package sorting for microfluidic logistics.
Movie S6. Application of the ferrobotic system for the implementation of a pipelined and automated bioassay.
References (*51*–*53*)

REFERENCES AND NOTES

1. J. Lambert, *How Robots Change the World* (Oxford Economics, 2019), vol. 43, pp. 5–8.
2. J.-T. Li, H.-L. Liu, Design optimization of amazon robotics. *Automat. Contr. Intel. Syst.* **4**, 48–52 (2016).
3. A. H. C. Ng, R. Fobel, C. Fobel, J. Lamanna, D. G. Rackus, A. Summers, C. Dixon, M. D. M. Dryden, C. Lam, M. Ho, N. S. Mufti, V. Lee, M. A. M. Asri, E. A. Sykes, M. D. Chamberlain, R. Joseph, M. Ope, H. M. Scobie, A. Knipes, P. A. Rota, N. Marano, P. M. Chege, M. Njuguna, R. Nzunza, N. Kisangau, J. Kiogora, M. Karuingi, J. W. Burton, P. Borus, E. Lam, A. R. Wheeler, A digital microfluidic system for serological immunoassays in remote settings. *Sci. Transl. Med.* **10**, eaar6076 (2018).
4. V. Srinivasan, V. K. Pamula, R. B. Fair, An integrated digital microfluidic lab-on-a-chip for clinical diagnostics on human physiological fluids. *Lab Chip* **4**, 310–315 (2004).
5. A. H. C. Ng, M. D. Chamberlain, H. Situ, V. Lee, A. R. Wheeler, Digital microfluidic immunocytochemistry in single cells. *Nat. Commun.* **6**, 7513 (2015).
6. A. R. Wheeler, H. Moon, C. A. Bird, R. R. O. Loo, C.-J. C. J. Kim, J. A. Loo, R. L. Garrell, Digital microfluidics with in-line sample purification for proteomics analyses with MALDI-MS. *Anal. Chem.* **77**, 534–540 (2005).
7. A. Stark, D. J. Shin, T.-H. Wang, A sample-to-answer droplet magnetofluidic assay platform for quantitative methylation-specific PCR. *Biomed. Microdevices* **20**, 31 (2018).
8. B. Wu, S. von der Ecken, I. Swyer, C. Li, A. Jenne, F. Vincent, D. Schmidig, T. Kuehn, A. Beck, F. Busse, H. Stronks, R. Soong, A. R. Wheeler, A. Simpson, Rapid chemical reaction monitoring by digital microfluidics-NMR: Proof of principle towards an automated synthetic discovery platform. *Angew. Chem. Int. Ed. Engl.* **58**, 15372–15376 (2019).
9. H. Ding, S. Sadeghi, G. J. Shah, S. Chen, P. Y. Keng, C.-J. C. J. Kim, R. M. van Dam, Accurate dispensing of volatile reagents on demand for chemical reactions in EWOD chips. *Lab Chip* **12**, 3331–3340 (2012).
10. M. Antfolk, T. Laurell, Continuous flow microfluidic separation and processing of rare cells and bioparticles found in blood – A review. *Anal. Chim. Acta* **965**, 9–35 (2017).
11. M. Karle, S. K. Vashist, R. Zengerle, F. von Stetten, Microfluidic solutions enabling continuous processing and monitoring of biological samples: A review. *Anal. Chim. Acta* **929**, 1–22 (2016).
12. D. Di Carlo, D. Irimia, R. G. Tompkins, M. Toner, Continuous inertial focusing, ordering, and separation of particles in microchannels. *Proc. Natl. Acad. Sci. U.S.A.* **104**, 18892–18897 (2007).
13. M. Abdelgawad, A. R. Wheeler, The digital revolution: A new paradigm for microfluidics. *Adv. Mater.* **21**, 920–925 (2009).
14. M. G. Pollack, R. B. Fair, A. D. Shenderov, Electrowetting-based actuation of liquid droplets for microfluidic applications. *Appl. Phys. Lett.* **77**, 1725 (2000).
15. K. Choi, A. H. C. Ng, R. Fobel, A. R. Wheeler, Digital Microfluidics. *Annu. Rev. Anal. Chem.* **5**, 413–440 (2012).
16. M. Mibus, G. Zangari, Performance and reliability of electrowetting-on-dielectric (EWOD) systems based on tantalum oxide. *ACS Appl. Mater. Interfaces* **9**, 42278–42286 (2017).
17. Y. Zhang, N.-T. Nguyen, Magnetic digital microfluidics - A review. *Lab Chip* **17**, 994–1008 (2017).
18. J. Pipper, Y. Zhang, P. Neuzil, T.-M. Hsieh, Clockwork PCR including sample preparation. *Angew. Chem. Int. Ed. Engl.* **47**, 3900–3904 (2008).
19. W. H. Koh, K. S. Lok, N.-T. Nguyen, A digital micro magnetofluidic platform for lab-on-a-chip applications. *J. Fluids Eng.* **135**, 021302 (2013).
20. U. Lehmann, C. Vandevyver, V. K. Parashar, M. A. M. Gijs, Droplet-based DNA purification in a magnetic lab-on-a-chip. *Angew. Chem. Int. Ed. Engl.* **45**, 3062–3067 (2006).
21. C.-H. Chiou, D. J. Shin, Y. Zhang, T.-H. Wang, Topography-assisted electromagnetic platform for blood-to-PCR in a droplet. *Biosens. Bioelectron.* **50**, 91–99 (2013).
22. M. Egeblad, Z. Werb, New functions for the matrix metalloproteinases in cancer progression. *Nat. Rev. Cancer* **2**, 161–174 (2002).
23. L. Sevenich, J. A. Joyce, Pericellular proteolysis in cancer. *Genes Dev.* **28**, 2331–2347 (2014).
24. W. C. Parks, C. L. Wilson, Y. S. López-Boado, Matrix metalloproteinases as modulators of inflammation and innate immunity. *Nat. Rev. Immunol.* **4**, 617–629 (2004).
25. I. Swyer, R. Fobel, A. R. Wheeler, Velocity saturation in digital microfluidics. *Langmuir* **35**, 5342–5352 (2019).
26. J. Li, N. S. Ha, T. Liu, R. M. van Dam, C.-J. Kim, Ionic-surfactant-mediated electro-dewetting for digital microfluidics. *Nature* **572**, 507–510 (2019).
27. S. Kahkeshani, J. E. Kong, Q. Wei, D. Tseng, O. B. Garner, A. Ozcan, D. Di Carlo, Ferrodrop dose-optimized digital quantification of biomolecules in low-volume samples. *Anal. Chem.* **90**, 8881–8888 (2018).

28. S. Kahkeshani, D. Di Carlo, Drop formation using ferrofluids driven magnetically in a step emulsification device. *Lab Chip* **16**, 2474–2480 (2016).
29. Y. Cheng, X. Ye, Z. Ma, S. Xie, W. Wang, High-throughput and clogging-free microfluidic filtration platform for on-chip cell separation from undiluted whole blood. *Biomicrofluidics* **10**, 014118 (2016).
30. X. Qiu, J. A. Lombardo, T. M. Westerhof, M. Pennell, A. Ng, H. Alshetaiwi, B. M. Luna, E. L. Nelson, K. Kessenbrock, E. E. Hui, J. B. Haun, Microfluidic filter device with nylon mesh membranes efficiently dissociates cell aggregates and digested tissue into single cells. *Lab Chip* **18**, 2776–2786 (2018).
31. B. Bhattacharjee, S. A. Vanapalli, Electrocoalescence based serial dilution of microfluidic droplets. *Biomicrofluidics* **8**, 044111 (2014).
32. R. Tewhey, J. B. Warner, M. Nakano, B. Libby, M. Medkova, P. H. David, S. K. Kotsopoulos, M. L. Samuels, J. B. Hutchison, J. W. Larson, E. J. Topol, M. P. Weiner, O. Harismendy, J. Olson, D. R. Link, K. A. Frazer, Microdroplet-based PCR enrichment for large-scale targeted sequencing. *Nat. Biotechnol.* **27**, 1025–1031 (2009).
33. D. J. Eastburn, A. Sciambi, A. R. Abate, Picoinjection enables digital detection of RNA with droplet rt-PCR. *PLOS One.* **8**, e62961 (2013).
34. A. R. Wheeler, H. Moon, C.-J. Kim, J. A. Loo, R. L. Garrell, Electrowetting-based microfluidics for analysis of peptides and proteins by matrix-assisted laser desorption/ionization mass spectrometry. *Anal. Chem.* **76**, 4833–4838 (2004).
35. A. H. C. Ng, B. B. Li, M. D. Chamberlain, A. R. Wheeler, Digital microfluidic cell culture. *Annu. Rev. Biomed. Eng.* **17**, 91–112 (2015).
36. R. Cole, Parallel merge sort. *SIAM J. Comput.* **17**, 770–785 (1988).
37. M. Dhar, J. N. Lam, T. Walser, S. M. Dubinett, M. B. Rettig, D. Di Carlo, Functional profiling of circulating tumor cells with an integrated vortex capture and single-cell protease activity assay. *Proc. Natl. Acad. Sci. U.S.A.* **115**, 9986–9991 (2018).
38. R. E. Vandenbroucke, L. Dejager, C. Libert, The first MMP in sepsis. *EMBO Mol. Med.* **3**, 367–369 (2011).
39. G. Martin, V. Asensi, A. H. Montes, J. Collazos, V. Alvarez, J. A. Carton, F. Taboada, E. Valle-Garay, Role of plasma matrix-metalloproteases (MMPs) and their polymorphisms (SNPs) in sepsis development and outcome in ICU patients. *Sci. Rep.* **4**, 5002 (2014).
40. I. Vanlaere, C. Libert, Matrix metalloproteinases as drug targets in infections caused by gram-negative bacteria and in septic shock. *Clin. Microbiol. Rev.* **22**, 224–239 (2009).
41. L. Nissinen, V.-M. Kähäri, Matrix metalloproteinases in inflammation. *Biochim. Biophys. Acta.* **1840**, 2571–2580 (2014).
42. L. Ravanti, V. M. Kähäri, Matrix metalloproteinases in wound repair (review). *Int. J. Mol. Med.* **6**, 391–407 (2000).
43. A. Gutiérrez-Fernández, M. Inada, M. Balbín, A. Fueyo, A. S. Pitiot, A. Astudillo, K. Hirose, M. Hirata, S. D. Shapiro, A. Noël, Z. Werb, S. M. Krane, C. López-Otín, X. S. Puente, Increased inflammation delays wound healing in mice deficient in collagenase-2 (MMP-8). *FASEB J.* **21**, 2580–2591 (2007).
44. E. M. Miller, A. R. Wheeler, A Digital microfluidic approach to homogeneous enzyme assays. *Anal. Chem.* **80**, 1614–1619 (2008).
45. D. H. Nam, X. Ge, Development of a periplasmic FRET screening method for protease inhibitory antibodies. *Biotechnol. Bioeng.* **110**, 2856–2864 (2013).
46. I. I. Bogoch, H. C. Koydemir, D. Tseng, R. K. D. Ephraim, E. Duah, J. Tee, J. R. Andrews, A. Ozcan, Evaluation of a mobile phone-based microscope for screening of Schistosoma haematobium infection in rural Ghana. *Am. J. Trop. Med. Hyg.* **96**, 1468–1471 (2017).
47. M. R. Bashir, L. Bhatti, D. Marin, R. C. Nelson, Emerging applications for ferumoxytol as a contrast agent in MRI. *J. Magn. Reson. Imaging* **41**, 884–898 (2015).
48. M. Lu, M. H. Cohen, D. Rieves, R. Pazdur, FDA report: Ferumoxytol for intravenous iron therapy in adult patients with chronic kidney disease. *Am. J. Hematol.* **85**, 315–319 (2010).
49. H. Lin, Y. Zhao, S. Lin, B. Wang, C. Yeung, X. Cheng, Z. Wang, T. Cai, W. Yu, K. King, J. Tan, K. Salahi, H. Hojaiji, S. Emaminejad, A rapid and low-cost fabrication and integration scheme to render 3D microfluidic architectures for wearable biofluid sampling, manipulation, and sensing. *Lab Chip* **19**, 2844–2853 (2019).
50. H. Lin, H. Hojaiji, S. Lin, C. Yeung, Y. Zhao, B. Wang, M. Malige, Y. Wang, K. King, W. Yu, J. Tan, Z. Wang, X. Cheng, S. Emaminejad, A wearable electrofluidic actuation system. *Lab Chip* **19**, 2966–2972 (2019).
51. N. Pamme, Magnetism and microfluidics. *Lab Chip* **6**, 24–38 (2006).
52. Z. Long, A. M. Shetty, M. J. Solomon, R. G. Larson, Fundamentals of magnet-actuated droplet manipulation on an open hydrophobic surface. *Lab Chip* **9**, 1567–1575 (2009).
53. N.-T. Nguyen, A. Beyzavi, K. M. Ng, X. Huang, Kinematics and deformation of ferrofluid droplets under magnetic actuation. *Microfluid. Nanofluid.* **3**, 571–579 (2007).

Acknowledgments: We thank the UCLA Nanoelectronics Research Facility (NRF) for providing access to device fabrication equipment and J. Shao at UCLA Department of Radiological Science for supplying ferumoxytol materials. **Funding:** This work was supported by S.E.'s startup package provided by the UCLA Henry Samueli School of Engineering and Applied Sciences. D.D. and Y.W. acknowledge support from the NSF TANMS ERC (award no. 1160504).
Author contributions: S.E., D.D., W.Y., H.L., and Y.W. conceived the general ferrobot idea and contributed to the design of experiments. W.Y., H.L., X.H., N.C., K.S., and J.T. conducted the device fabrication and characterization. Y.W. designed and validated the quantitative assay framework. W.Y., H.L., and N.C. designed the PCB circuit. W.Y., H.L., Y.W., and D.L. performed bioassays and fluorescent imaging. Y.W. developed the imaging algorithm. W.Y., H.L., Y.W., X.H., N.C., K.S., D.L., and B.C. contributed to analytical tools and data analysis. S.E., D.D., W.Y., H.L., Y.W., and C.Y. drafted the manuscript, and all the authors provided feedback. **Competing interests:** S.E., D.D., W.Y., H.L., and Y.W. are inventors on a provisional patent application (U.S. Prov App No. 62/924,505) on the presented technology. The other authors declare that they have no competing interests. **Data and materials availability:** All data needed to evaluate the conclusions in the paper are present in the paper and/or the Supplementary Materials. Additional data related to this paper may be requested from the authors.

Submitted 4 December 2019
Accepted 5 February 2020
Published 26 February 2020
10.1126/scirobotics.aba4411

Citation: W. Yu, H. Lin, Y. Wang, X. He, N. Chen, K. Sun, D. Lo, B. Cheng, C. Yeung, J. Tan, D. Di Carlo, S. Emaminejad, A ferrobotic system for automated microfluidic logistics. *Sci. Robot.* **5**, eaba4411 (2020).

Science Robotics

A ferrobotic system for automated microfluidic logistics

Wenzhuo Yu, Haisong Lin, Yilian Wang, Xu He, Nathan Chen, Kevin Sun, Darren Lo, Brian Cheng, Christopher Yeung, Jiawei Tan, Dino Di Carlo, and Sam Emaminejad

Sci. Robot. **5** (39), eaba4411. DOI: 10.1126/scirobotics.aba4411

Science Robotics (ISSN 2470-9476) is published by the American Association for the Advancement of Science. 1200 New York Avenue NW, Washington, DC 20005. The title *Science Robotics* is a registered trademark of AAAS.